J. Ocean Univ. China (Oceanic and Coastal Sea Research)
https://doi.org/10.1007/s11802-023-5172-x
ISSN 1672-5182, 2023 22 (1): 9-20
http://www.ouc.edu.cn/xbywb/
E-mail:xbywb@ouc.edu.cn

L-Band Analysis of the Effects of Oil Slicks on Sea Wave Characteristics

JIANG Tao[1)], SHAO Weizeng[1), 2), 3), *], HU Yuyi[1)], ZHENG Gang[2)], and SHEN Wei[4), *]

1) *College of Marine Sciences*, *Shanghai Ocean University*, *Shanghai* 201306, *China*
2) *State Key Laboratory of Satellite Ocean Environment Dynamics*, *Ministry of Natural Resources*, *Hangzhou* 310012, *China*
3) *National Satellite Ocean Application Service*, *Ministry of Natural Resources*, *Beijing* 100081, *China*
4) *China Waterborne Transport Research Institute*, *Ministry of Transport*, *Beijing* 100088, *China*

(Received August 24, 2021; revised October 27, 2021; accepted November 23, 2021)

Abstract The purpose of this study was to investigate the characteristics of sea surface waves as they pass through oil slicks. The parameterized first-guess spectrum method (PFSM) theory-based wave retrieval algorithm was applied to 20 images of horizontal-horizontal (HH) polarization obtained using the phased-array L-band synthetic aperture radar (SAR) (PALSAR) on the Advanced Land Observing Satellite (ALOS-1). The images were collocated with simulations from the WAVEWATCH-III (WW3) model in a 0.1° grid using the European Centre for Medium-Range Weather Forecasts (ECMWF) reanalysis (ERA-5) winds data as the forcing field. The validation of the model-simulated significant wave height (SWH) against the measurements from the Jason-2 altimeter produced a 0.66 m root mean square error (RMSE) for the SWH, with a coefficient (COR) 0.74. In this sense, the WW3-simulated waves were reliable for our work. A comparison between the SAR retrieval results and the WW3 simulations was performed using the dataset for the regions without oil slicks, which produced a 0.34 m RMSE for the SWH, with a COR of 0.79, which is less than a the RMSE of 0.52 m and the COR of 0.70 for the regions with oil slicks. Moreover, it was found that the SAR-derived SWHs were significantly underestimated by about 0.2 m in the areas with oil slicks. This difference is probably due to the underestimation of the SAR-derived wind speeds at moderate wind speeds (*i.e.*, at wind speeds of greater than 5 m s^{-1}). An additional analysis compared the SAR-derived wave spectra with those from the WW3 model as waves passed through the oil slicks. The interesting finding is that the wave energy at short wave lengths (about 30 m) is reduced by the oil slicks, causing the movement of the dominant wave spectrum to shift to longer wave lengths (about 80 m).

Key words wind; wave; WAVEWATCH-III; ALOS-1 PALSAR; oil slicks

1 Introduction

Waves play an important role in atmospheric-marine interactions. They affect economic activities in near-shore waters, especially during tropical cyclones (Hu *et al.*, 2020a). Strong waves are a danger to tankers and oil platforms and can result in accidental spills (Yang *et al.*, 2021). With the development of remote-sensing techniques, spilled oil can be easily detected by optical and microwave satellites (Esaias *et al.*, 1998). However, oil slicks have a great influence not only on the marine ecological environment but also on sea surface dynamics. An accurate understanding of sea surface dynamics is essential for predicting the movement of oil spills using numerical models (Yang *et al.*, 2021). Until recently, few studies had been conducted concerning the characteristics of waves in the presence of oil slicks, finding that the damping of the gravity-capillary waves by oil slicks depends on the thickness of the oil slick (Ermakov *et al.*, 2012).

Synthetic Aperture Radar (SAR) has the ability to measure sea surface parameters (basically wind and waves) over a large area with a high spatial resolution, *e.g.*, a 100 km swath with up to 1 m pixel resolution for Chinese civilian SAR, denoted as Gaofen-3 (Shao *et al.*, 2018c). The Geophysical Model Function (GMF) CMOD (C-band, 5 cm wavelength) and XMOD (X-band, 3 cm wavelength) families, *e.g.*, CMOD4 (Stoffelen and Anderson, 1997), CMOD-IFR2 (Quilfen *et al.*, 1998), CMOD5/CMOD5.N (Hersbach *et al.*, 2007; Hersbach, 2010), C-SARMOD (Mouche *et al.*, 2005; Shao *et al.*, 2021), and XMOD2 (Li and Lehner, 2014), are popular for wind retrieval from C-band SAR for the co-polarization channel. The phased-array L-band (24 cm wavelength) synthetic aperture radar onboard the Advanced Land Observing Satellite (ALOS-1), for which the GMF for the L-band (Meng *et al.*, 2022) is called LMOD, is specifically designed for wind retrieval (Isoguchi and Shimada, 2009). Because it is difficult to obtain a wind vector that includes both the wind speed and direction by solving the individual GMF, prior information about the wind direction from a reanalysis system

* Corresponding authors. E-mail: wzshao@shou.edu.cn
E-mail: shenwei@wti.ac.cn

(*e.g.*, the European Centre for Medium-Range Weather Forecasts (ECMWF)) (Shao *et al.*, 2014a) is often used. The evaluation of the wind retrieval using co-polarized (vertical-vertical (VV) or horizontal-horizontal (HH)) SAR images has been well studied, and it has been concluded that the accuracy for C-band SAR is about $2\,\mathrm{m\,s^{-1}}$, *e.g.*, ERS-1 (Lehner *et al.*, 1998), Sentinel-1 (Monaldo *et al.*, 2016), and RADARSAR-1/2 (Yang *et al.*, 2011). This result was also found for L-band SAR, such as the Japanese Earth Resources Satellite-1 (JERS) (Shimada *et al.*, 2003) by applying the GMF LMOD. It should be noted that the LMOD was initially developed for HH-polarized SAR, and therefore, the polarization ratio (PR) model (Li *et al.*, 2018) is not necessary when applying the VV-polarized GMF for the C- and X-band SAR.

SAR backscattering is distorted by the azimuthal (defined as the satellite flight direction) Doppler shift caused by the relative movement between the satellite platform and the sea surface (Honkavaara *et al.*, 2013). This nonlinear effect, which is known as the velocity bunching mechanism (Alpers *et al.*, 1981; Lyzenga, 2002), is stronger than the tilt modulation (Lyzenga, 1986) and hydrodynamic modulation (Feindt *et al.*, 1986). Under these circumstances, short waves with a wavelength smaller than the critical cutoff value are undetectable using SAR. Typically, wave spectrum retrieval algorithms for co-polarized SAR consist of two types: SAR imaging mechanism-based algorithms and empirical approaches (Shao *et al.*, 2015). The theory-based co-polarization algorithms include the Max-Planck Institute (MPI) algorithm (Hasselmann and Hasselmann, 1991), the semi-parametric retrieval algorithm (SPRA) (Mastenbroke and Valk, 2000), the parameterized first-guess spectrum method (PFSM) (Sun and Kawamura, 2009), and the partition rescaling and shift algorithm (PARSA) (Shulz-Stellenfleth *et al.*, 2005). One difficulty with these algorithms is the necessity of a first-guess wave spectrum in which the true wave spectrum is inverted by minimizing the cost function in order to resolve the modulation transfer function (MTF) of the non-linear velocity bunching. In practice, the waves simulated using a numerical wave model, such as the WAve model (WAM) (The Wamdi Group, 1988) in the MPI algorithm, and an empirical wind-sea model, such as the Joint North Sea Wave Project (JONSWAP) model (Hasselmann, 1973) in the SPRA algorithm, can be used as the first-guess wave spectrum. Although the SPRA algorithm is more commonly applied (Voorrips *et al.*, 2001), it has been found that the error is inevitably included in the scheme of the SPRA algorithm due to the fact that the difference between the retrieved wind-sea mapping spectrum and the observed SAR spectrum is supposedly mapped to the swell, which usually contains the error of the wind-sea retrieval. To overcome this limitation, information about the wind-sea and swell in a SAR spectrum is first separated using the SAR-derived winds and satellite parameters. The best fit parameters for producing the first-guess wind-sea spectrum, *e.g.*, the dominant wave phase velocity and wave propagation direction, are optimally selected in the empirical JONSWAP model. The PFSM algorithm has been successfully used for wave retrieval from Sentinel-1 (Ding *et al.*, 2019) and Gaofen-3 (Zhu *et al.*, 2019) SAR images. Using the backscattering signal in quad-polarization (basically VV, HH, vertical-horizontal (VH)), the wave retrieval algorithm for quad-polarized SAR initially proposed by Shao *et al.* (2014a) has been proven to validate the wave retrieval from a number of quad-polarized RADARSAT-2 images against moored buoys (Zhang *et al.*, 2010). In a recent study (He *et al.*, 2006), the quad-polarization wave retrieval algorithm was implemented for GF-3 SAR data acquired in wave mode, revealing that the inverted SWH tends to become saturated at SWHs of up to 1.4 m due to the low SAR backscattering signals of the cross-polarization channel (Migliaccio *et al.*, 2019).

The empirical approach is another option for SAR wave retrieval. Several studies have focused on exploring models that allow the direct retrieval of the SWH without calculating complex MTFs for each modulation, *e.g.*, CWAVE for the C-band (Schulz-Stellenfleth *et al.*, 2007; Li *et al.*, 2011) and XWAVE for the X-band (Pleskachevsky *et al.*, 2016). The principle behind the CWAVE and XWAVE families is that the SAR imaging parameters are determined by the sea state. That is, the mapping mechanism for SAR can be bypassed to some extent by building an empirical function. One drawback of the empirical approach is the intricate variables involved in the formulas selected by different researchers, *e.g.*, a set of orthonormal functions in a two-dimensional SAR spectrum and the azimuthal cutoff length because the cutoff length is proportional to the second moment of the wave spectrum (Grieco *et al.*, 2016). Empirical models need to be adopted for specific SAR sensors, *e.g.*, CWAVE_ERS (Schulz-Stellenfleth *et al.*, 2007) for the ERS-1/2 SAR, CWAVE_ENV (Li *et al.*, 2011) for the ENVISAT-ASAR, CWAVE_S1 for the European Sentinel-1 (S-1) SAR (Stopa and Mouche, 2017), and CSAR_WAVE for the Gaofen-3 (Sheng *et al.*, 2018). Empirical models cannot be applied in the presence of oil slicks due to the effects induced by the spilled oil.

Oil slicks are detected more easily in C-band SAR images than in L-band SAR images (Zheng *et al.*, 2017) because sea surface gravity waves are sensitive to microwaves in the C-band. Therefore, the analysis on the effects of oil slicks on sea wave characteristics for L-band SAR could improve the accuracy of oil slick detection. In this study, 20 ALOS-1 PALSAR images in HH-polarization in which oil slicks created by ships could be seen were used to analyze the retrieval of wave characteristics using a PFSM algorithm. The purpose this study was to investigate the performance of the wave spectrum compared with those simulated using the WW3 model while passing oil slicks under various sea states. The remainder of this paper is organized as follows: the datasets are briefly described in Section 2, *e.g.*, ALOS-1 PALSAR images, measurements from the Advanced Scatterometer (ASCAT) and Jason-2 altimeter, and the settings of the WW3 model. Section 3 introduces the methodology of the existing theory-based PFSM algorithm. Section 4 presents the validation of the wind and SWH data retrieved using the PFSM algorithm. This section also contains a discussion of the

characteristics of the wave spectra as they pass through the oil slicks. The conclusions are summarized in Section 5.

2 Description of Datasets

A total of 20 ALOS-1 PALSAR images containing oil slicks were available for use in this study. The SAR products were preceded to be Level-1.5 with the Fine Mode (FM) for the HH-polarization channel from March 2007 to May 2008. Fig.1 shows the geographic locations of the PALSAR images overlain with the water depth data from the General Bathymetric Chart of the Oceans (GEBCO) (Jakobsson and Macnab, 2006). The black rectangles represent the spatial coverage of the collected images. The calibration method in Eq. (1) was used to collect the L-band HH-polarized normalized radar cross section (NRCS):

$$\sigma^0_{\mathrm{HH}}[\mathrm{dB}] = 10\times\log_{10}(DN^2) + CF\ , \qquad (1)$$

where DN is the pixel intensity of the four-look 16-bit PALSAR images, and CF is a calibration factor, which is assumed to have a constant value of −83 dB (Shimada *et al.*, 2009). The radiometric accuracy of the PALSAR was determined to be 0.64 dB, and the noise-equivalent NRCS, which was empirically estimated as the minimum area-averaged NRCS from the FM data, is approximately equal to −32 dB. Fig.2 shows a calibrated quick-look of a PALSAR FM Geo-coded image acquired in the East China Sea at 14:20 UTC on July 22, 2007, in which rectangles A and B represent the geographic locations of the oil slicks. The spatial coverage of the SAR image ranges from 34.87˚N, 121.61˚E, to 35.46˚N, 122.41˚E, and the incidence angle ranges from 36.74˚ to 40.43˚. The dark patches marked in Fig.2 are caused by the ships monitored by the Automatic identification System (AIS).

To confirm the accuracy of the SAR-derived wind speeds, measurements were collected from the ASCAT 25 km products provided by the Royal Netherlands Meteorological Institute (Bi *et al.*, 2011). The ASCAT scatterometer aboard the MetOp-A satellite operates in the C-band. Therefore, the winds were previously calculated based on the GMF CMOD5N, and the newly released products are based on the CMOD7 (Stoffelen *et al.*, 2017). Because the local observation time of the MetOp-A satellite is relatively close to that of ALOS-1, the matchups between the ASCAT and PALSAR have small time gaps (<15 min) and are reliable for validation. The ASCAT data are the global wind speeds and directions on a 25 km grid. A symmetric calibration was conducted *via* comparison of the ASCAT and more than 10000 ECMWF reanalysis (ERA-5) winds, yielding root-mean-square errors (RMSEs) of 1.26 m s^{-1} and about 15˚ for the wind speed and wind direction, respectively (Verspeek *et al.*, 2010). Fig.3a shows the ASCAT-measured wind map at 13:30 UTC on August 15, 2008. Because the spatial resolution of the ASCAT is relatively coarse, which results in insufficient matchups with the SAR-derived winds, *e.g.*, no available ASCAT winds for the case in Fig.2, the ERA-5 winds for a 0.25˚ grid with an interval of 1 h were also used to validate the SAR-derived winds, especially in the regions with oil slicks. A wind map from ERA-5 at 14:30 UTC on August 15, 2008, is shown in Fig.3b.

Waves simulated using a third-generation numerical

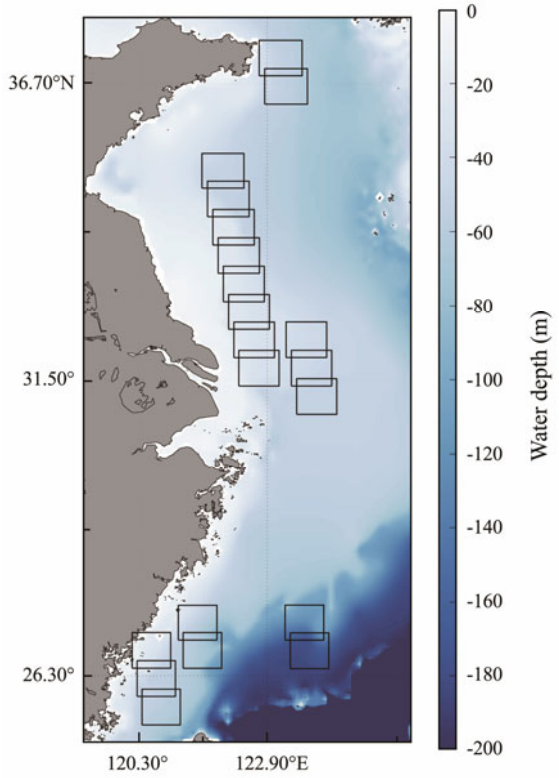

Fig.1 The geographic locations of the Advanced Land Observing Satellite phased-array L-band synthetic aperture radar (SAR) (PALSAR) images overlain with the water depths, in which the black rectangles represent the spatial coverage of the collected images.

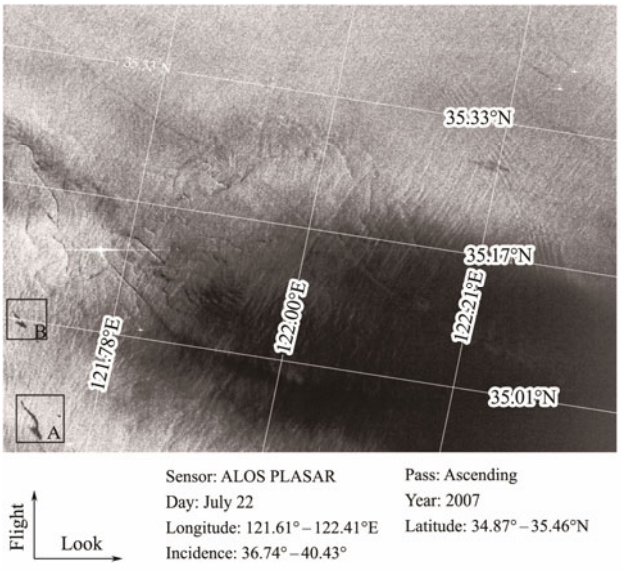

Fig.2 The calibrated quick-look of a horizontal-horizontal (HH) polarized PALSAR Geo-coded image acquired in the East China Sea at 14:20 UTC on July 22, 2007. Rectangles A and B represent the geographic locations of the oil slicks.

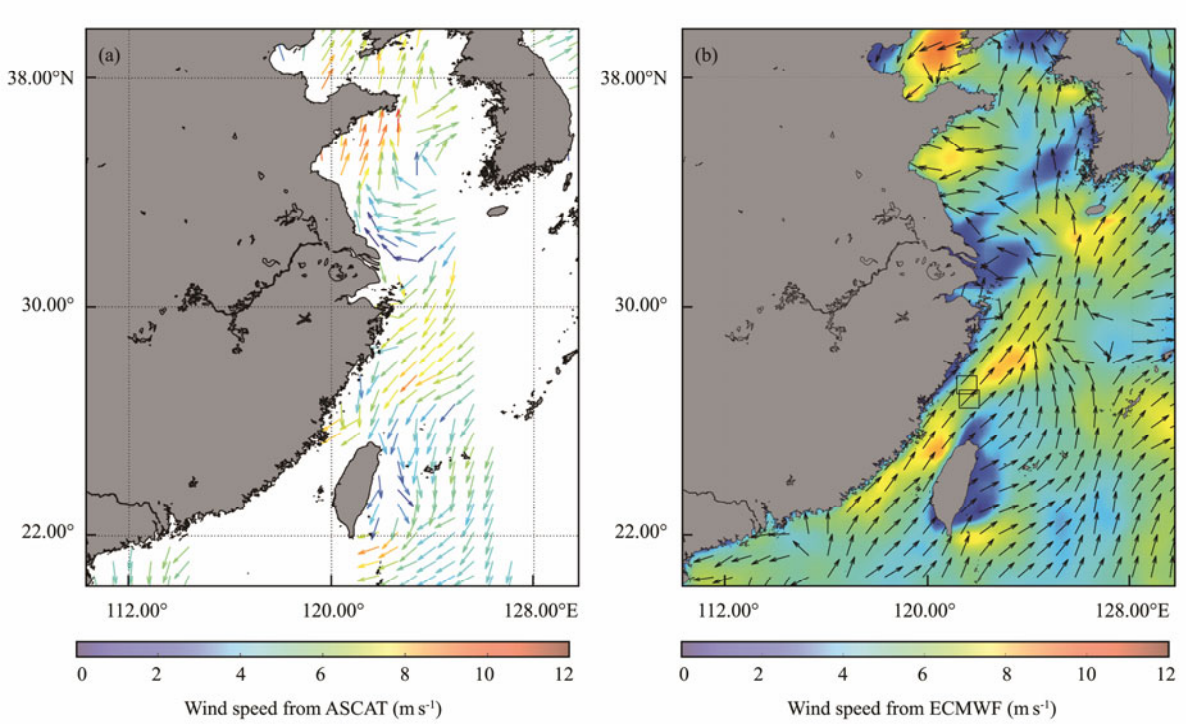

Fig.3 (a) The 0.25˚ grid wind map from the Advanced Scatterometer (ASCAT) at 13:30 UTC on August 15, 2008. (b) The 0.125˚ wind map from the European Centre for Medium-Range Weather Forecasts (ECMWF) reanalysis (ERA-5) at 14:30 UTC on August 15, 2008.

model, denoted WAVEWATCH-III (version 6.07) (Tolman and Chalikov, 1996), were also collocated from the PALSAR images. The WW3 model has performed well in a global wave distribution analysis, even in areas with tropical cyclones (Hu *et al.*, 2020b) and in the Arctic Ocean (Shao *et al.*, 2022). The forcing field was the 0.25˚ gridded ERA-5 reanalysis winds at an interval of 1 h, and the water depths were derived from the GEBCO bathymetric data at 30 arc grids (about 1 km spatial resolution in the horizontal direction). The computation settings were as follows: The frequency bins ranged logarithmically from 0.04118 to 0.7186 with an interval of 0.1; the spatial propagation was characterized by 300 s time steps in both the longitudinal and latitudinal directions; the temporal resolution was 30 min; the spatial grid resolution was a 0.2˚ grid. The SWH product from the Jason-2 altimeter, which is a reliable remote-sensed source for sea height monitoring, was used to validate the WW3-simulation results. The switches described by the Wamdi Group (1988) illustrate the physical dynamics, which were as follows: The ST2 package was used for the input/dissipation source terms; the TR1 package was used for the triad wave-wave interactions; the GMD2 package was used for the quadruplet wave-wave interactions; the FLD2 package was used for the wave breaking. Fig.4 shows the WW3-simulated SWH map overlain with the footprints of the Jason-2 altimeter at 17:00 UTC on August 15, 2008. The statistical analysis of the SWH in August 2008 yielded a 0.66 m RMSE with a 0.74 correlation coefficient (COR) between the WW3-simulated SWH and the measurements from the footprint of the Jason-2 altimeter (Fig.5) (Shao *et al.*, 2018a, 2018b). Based on these results, we believe that waves simulated using the WW3 model are suitable for this study.

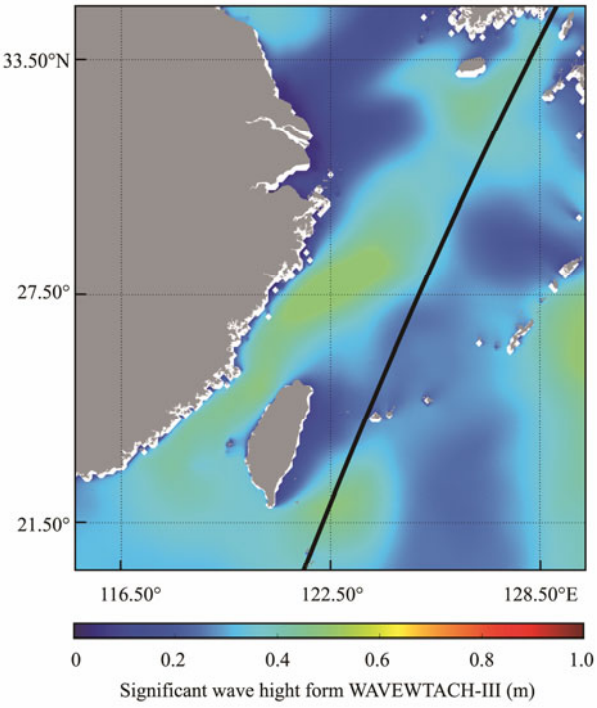

Fig.4 The simulated SWH map from the WAVEWATCH-III (WW3) model overlain on the footprints of the Jason-2 altimeter at 17:00 UTC on August 15, 2008.

3 Methodology

In this section, the wind retrieval GMF in the L-band,

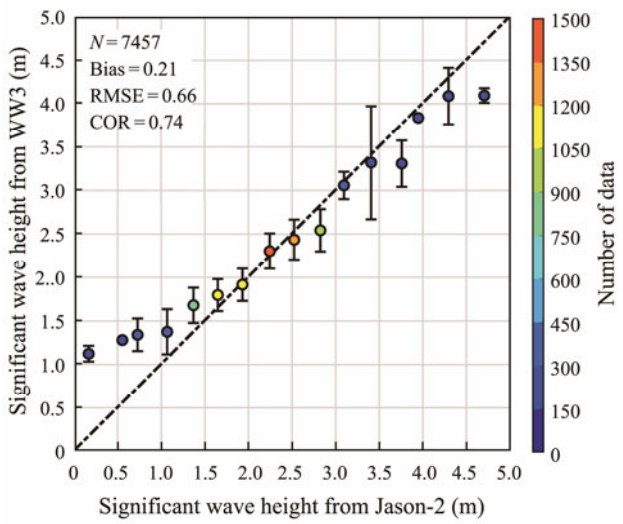

Fig.5 Comparison of the SWH from the WW3 model with the collocated matchups from the Jason-2 altimeter in August 2008.

denoted as LMOD, is briefly described. Next, the scheme of the wave retrieval PFSM algorithm is discussed in detail. The comparison between the SWHs simulated using the WW3 model and the collocated measurements from the Jason-2 altimeter are also presented.

3.1 GMF LMOD

Prior information about the wind speed is necessary for the PFSM algorithm. The wind retrieval GMF in the L-band, herein denoted as LMOD, has been described by Hersbach *et al.* (2007). The LMOD function correlating a wind vector and NRCS has the following general formula:

$$\sigma^0_{\mathrm{HH}} = B_0(U_{10},\theta)\times \left(1+B_1(U_{10},\theta)\times\cos\varphi+B_2(U_{10},\theta)\times\cos 2\varphi\right), \quad (2)$$

where σ^0_{HH} is the SAR-measured NRCS, φ is the wind direction relative to the radar look, the coefficients B_n (U_{10}, θ) (n=0, 1, 2) are the functions of the wind speed measured at 10 m above the sea surface, and U_{10} is the radar incidence angle θ ($36.5^\circ<\theta<40.5^\circ$), which are tuned using the collocated scatterometer wind products and the SAR measurements. Although there are visible wind streaks in some SAR images (Alpers and Brummer, 1994), most of the subscenes have no visible wind streaks. The image-detected directions have a 180° ambiguity. An auxiliary source, such as the ERA-5 winds on a 0.25° grid, can be used to remove this ambiguity.

In the entire image, there are n-element referred wind directions ϕ_k at locations (x_k, y_k). The weight radius R, defined as the maximum distance at which the local wind is affected by the surroundings, is assumed to be 5 km. For each sub-scene grid (x_i, y_j), ϕ_0 is the referred wind direction and ϕ_k is the known wind direction nearest to the grid (x_i, y_j). D_k is the spatial distance in km between grid (x_i, y_j) and grids (x_k, y_k), and $\Delta\phi_k$ ($=\phi_0-\phi_k$) is the difference between wind direction ϕ_0 and the individual referred wind direction ϕ_k. Finally, $\phi_{i,j}$ represents the SAR-derived wind direction at an about 1 km grid and is interpolated using Eq. (3) (Shao *et al.*, 2014b).

$$\phi_{i,j} = \phi_0 + \sum\nolimits_{k=1}^{n} \frac{D_k^2 - R^2}{D_k^2 + R^2}\Delta\phi_k \ . \quad (3)$$

3.2 PFSM Algorithm

The first wave retrieval scheme for SAR was the scheme proposed by Sun and Kawamura (2009), denoted as MPI. It considers the non-linear mapping mechanism velocity bunching, which is a critical modulation of the SAR mapping mechanism. The key of the MPI algorithm is to solve the MTF of the velocity bunching by minimizing the cost function J (Eq. (4)), which relies on the first-guess wave spectrum simulated using a numeric model:

$$J = \int (F_k - \bar{F}_k)^2 \mathrm{d}k + \mu\int\left(\frac{E_k - \bar{E}_k}{B - \bar{E}_k}\right)^2 \mathrm{d}k \ , \quad (4)$$

where

$$F_k = T_k^{\mathrm{SAR}} \times E_k \ , \quad (5a)$$

and

$$T_k^{\mathrm{SAR}} = T_k^{\mathrm{tilt}} + T_k^{\mathrm{hyd}} + T_k^{v} \ . \quad (5b)$$

Using the first-guess wave spectrum E_k and the wave number k, the mapped SAR spectrum $\bar{F}_k$ was calculated using Eq. (5a) and three MTFs T_k^{SAR}, where T_k^{tilt}, T_k^{hyd}, and T_k^{v} represent the MTFs of the tilt modulation, hydrodynamic modulation, and velocity bunching, respectively. The details of these MTFs are described by Alpers *et al.* (1981). F_k is the observed SAR spectrum, μ is the weighting coefficient, which reflects the relative confidence between the observed SAR spectrum and the first-guess wave spectrum (usually equivalent to 0.1Max(F_k)). The small positive number B was assumed to be 0.001 in order to ensure convergence of the variation solution. The optimal wave spectrum $\bar{E}_k$ was retrieved by solving Eq. (6) using an iterative technique (the details are described by Hasselmann and Hasselmann (1991)):

$$\frac{\partial J}{\partial \bar{E}_k} = 0 \ . \quad (6)$$

Although the SPRA algorithm follows the above scheme to obtain the wind-sea, the first-guess wave spectrum was produced using the empirical wind wave model JONSWAP, which is more convenient to apply than WAM. The swell mapped portion was assumed to be the difference between the retrieved wind-sea map and the observed spectrum. The inherent error of the swell was included in the retrieved wave spectrum, which combined the wind-sea with the swell. The advantage of the PFSM is that the SAR intensity spectrum is first divided into two mapping portions: non-linear and linear portions. The separation threshold of the wave-number k_s was calculated using Eq. (7), in which V is the satellite flight velocity, R is the satellite slant

range in each pixel, g is the gravitational acceleration (9.8 $\mathrm{m\,s^{-2}}$), and φ is the angle of the wave propagation direction relative to the radar look direction. Specifically, the method of retrieving the wind-sea spectrum E_k^w from the wind-sea mapping SAR spectrum F_k^w at wave-number $k \geq k_s$ follows the scheme of SPRA; while the swell spectrum E_k^s can be directly inverted from the swell mapping of the SAR spectrum F_k^s wave-number $k<k_s$ because the MTF of the velocity bunching can be ignored. Eq. (7) is as follows:

$$k_s = \left(\frac{2.87 g V^2}{R^2 U_{10}^4 \cos^2\varphi(\sin^2\varphi \sin^2\theta + \cos^2\varphi)} \right)^{0.33} . \quad (7)$$

The SAR-derived wave spectrum E_k ($= E_k^s + E_k^w$) is a composite of the wind-sea and swell retrieval. The SWH H_s was calculated by integrating a wave spectrum at all wave-numbers (Eq. (8); Hasselmann, 1973):

$$H_s = 4\sqrt{E_k \mathrm{d}k} . \quad (8)$$

4 Results

In this section, the theory-based PFSM algorithm is applied to 20 HH-polarization ALOS-1 PALSAR images, the retrieved wind speeds and SWHs are validated against the ASCAT-measured products and the simulations obtained using the WW3 model (Meng *et al.*, 2022), and the regions with oil-like patterns in the images are selected for analysis.

4.1 Comparison of Wind Retrieval

Before the wind retrieval process, the NRCSs were averaged for a region of about 1 $\mathrm{km^2}$ centered at the wind observation points in order to remove the effect of the small-scale phenomena, *e.g.*, waves and swells. Using prior information about the wind direction, the wind speeds at a spatial resolution of about 1 km were retrieved from the collected PALSAR images using the HH-polarized GMF LMOD. Fig.6 shows the SAR-derived wind map corresponding to the image in Fig.2. Wind speeds greater than 10 $\mathrm{m\,s^{-1}}$ are probably associated with the brightness in the image induced by ships. The accuracy of the wind retrieval from the PALSAR images has an RMSE of about 2 $\mathrm{m\,s^{-1}}$ based on validation against moored buoys (Hu *et al.*, 2020a). In this study, we simply repeated the comparison of the SAR-derived wind speeds with a few ASCAT winds during the periods in which the images were acquired (Fig.7). Generally, the analysis yielded a 1.82 $\mathrm{m\,s^{-1}}$ RMSE for the wind speed and a COR of 0.86. However, larger errors occurred at low wind speeds ($U_{10}<2\ \mathrm{m\,s^{-1}}$). This type of behavior has also been found for the implementation of the CMOD family for RADARSAR-2 SAR (Shao *et al.*, 2014b), and it is caused by weak backscattering at low wind speeds.

To study the influence of the oil slicks on the accuracy of the SAR-derived winds, ERA-5 winds at a 0.25° grid with an interval of 1 h were collocated with the collected images. Fig.8a shows that the RMSE of the wind speed is 1.90 $\mathrm{m\,s^{-1}}$ and the COR is 0.84 for the regions without oil slicks, whereas the RMSE and COR are 2.70 $\mathrm{m\,s^{-1}}$ and 0.64, respectively, for the regions with oil slicks Fig.8b. The underestimation of the SAR-derived wind speeds clearly occurred when the wind speeds were greater than 5 $\mathrm{m\,s^{-1}}$. However, the oil slicks likely have less influence on the wind retrieval at low wind speeds. In this sense, the SAR-derived winds are suitable for wave retrieval, although the accuracy of the winds is reduced by the modulation of the sea surface roughness induced by the oil slicks.

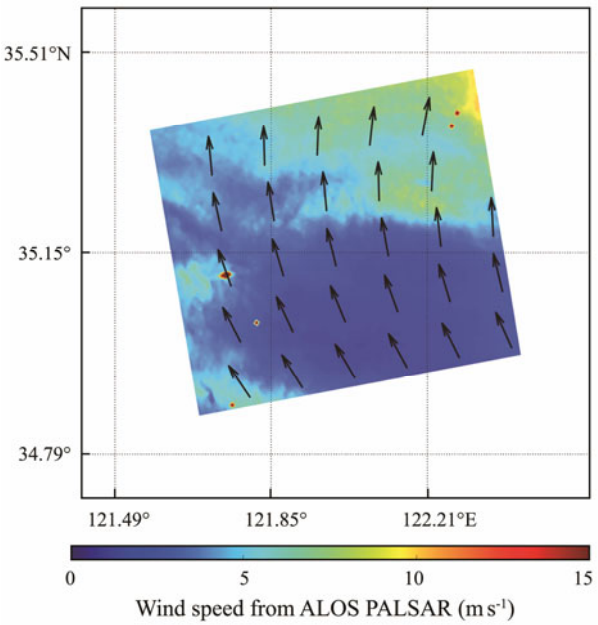

Fig.6 The wind map inverted from a HH-polarized PALSAR image using the geophysical model function LMOD, acquired in the East China Sea at 14:20 UTC on July 22, 2007.

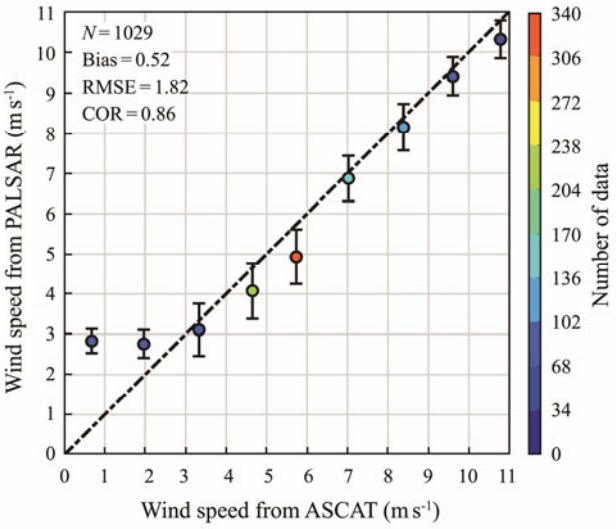

Fig.7 Comparison of the SAR-derived wind speeds with a few ASCAT winds for a 1 $\mathrm{m\,s^{-1}}$ bin between 0 and 11 m $\mathrm{s^{-1}}$.

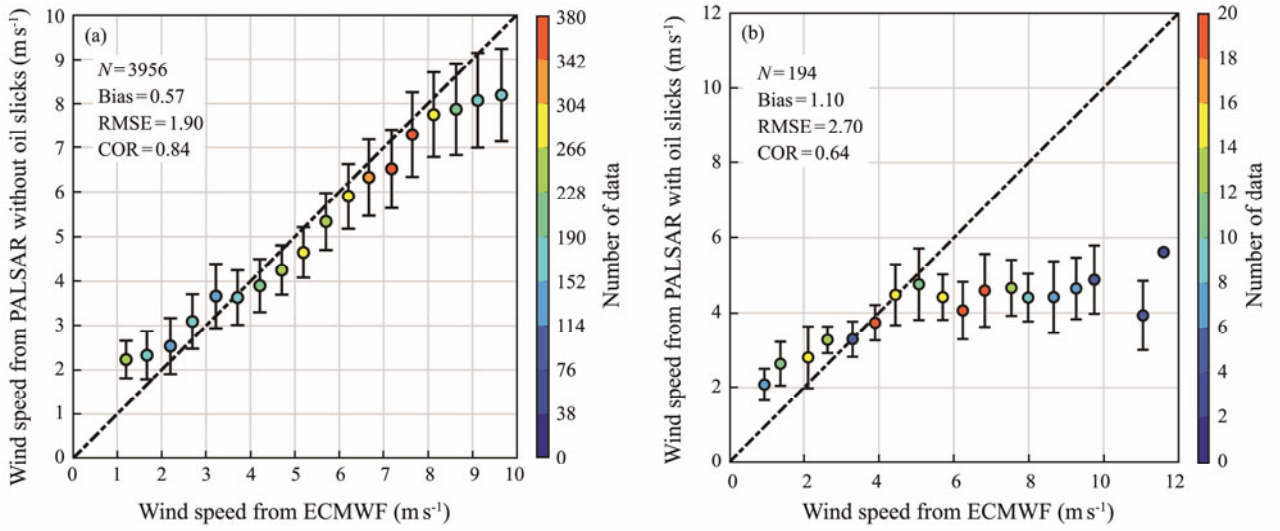

Fig.8 Comparisons between SAR-derived wind speeds from PALSAR images using LMOD with collocated ERA-5 wind speeds for a 0.5 m s^{-1} bin. (a) in the regions without oil slicks, and (b) in the regions with oil slicks.

4.2 Comparison of SWH Retrieval

As is described by Velotto *et al.* (2011), the oil slick's contribution to the SAR backscattering is smaller in the VV-polarization channel than in the HH-polarization channel because the NRCS is more sensitive to the non-Bragg backscattering caused by oil slicks (Kudryavtsev *et al.*, 2003). Under these circumstances, the wave retrieval using the HH-polarized SAR is supposedly distorted by the oil slicks. Therefore, an analysis of the SWH retrieval from the HH-polarized PALSAR images is presented here to assess the influence of the oil slicks.

The retrieved results of a sub-scene extracted from the images taken on June 16, 2007, at 05:43 UTC using the existing PFSM algorithm are presented as an example of the retrieved results. In this case, the SWH simulated using the WW3 model was 0.75 m. The geographic location is 120.48°E, 25.81°N, and the incidence angle is 37.15°. The quick-look image of the sub-scene covering the WW3 grids at 0.1° grids is shown in Fig.9a, and the corresponding two-dimensional SAR spectrum is shown in Fig.9b. The SAR-derived SWH was obtained using the PFSM algorithm was 0.39 m, and the retrieved one-dimensional wave spectrum (red dashed line) and the WW3-simulated wave spectrum (blue dashed line) are shown in Fig.9c.

All of the sub-scenes extracted from the PALSAR images were collocated with the simulations from the WW3 model in order to evaluate the accuracy of the SAR-derived SWH in the presence of oil slicks. Fig.10a shows that the SWH obtained using the PFSM algorithm has an RMSE of 0.34 m and a COR of 0.79 for the regions without oil slicks. This is less than the RMSE and COR of 0.52 m and 0.70, respectively, for the regions with oil slicks. In general, the SAR-derived SWH tends to be underestimated. This is caused by the underestimation of the SAR-derived wind speed (Fig.8). However, the larger difference (about 0.2 m) between the SAR-derived and WW3-simulated SWHs for the regions with oil slicks is clearly observed for SWHs of >0.7 m because the oil slicks dampen the sea surface roughness. The relationships between the incidence angle and the SAR-measured NRCS for the clean sea surface (red lines) and the oil-covered surface (black lines) were also analyzed. As can be seen from Fig.11a, the SAR-measured NRCS is significantly smaller than that in the clean region, *i.e.*, 2 dB at an incidence angle of 40°. For SWHs of >1 m (Fig.11b), the values of the SAR-measured NRCS with oil slicks are close to those for the clean sea surface, indicating that oil slicks are difficult to detect under such conditions. This type of behavior is consistent with the findings of Meng *et al.* (2022).

The PALSAR images taken on July 17, 2017, at 14:14 UTC were selected to analyze the results of the wave retrieval as the waves passed through the oil slicks (Fig.12). Three profiles passed through the oil slicks induced by ships, *i.e.*, A–C, D–F, and G–I. The oil slicks were particularly pronounced at locations B, E, and H. Fig.13 shows the retrieved results of the SAR-derived wave spectra obtained using the PFSM and the collocated wave spectra from the WW3 model, in which (a)–(i) correspond to A–I. Generally, the patterns of the SAR-derived wave spectra are consistent with the WW3-simulated wave spectra in the regions without oil slicks. It is not surpriseing that the normalized energy density from the SAR-derived wave spectrum is significantly reduced in the regions with oil slicks. In this case, the oil slicks likely dampen the short waves at wave numbers of 0.2 rad m^{-1} (wavelengths of about 30 m), causing a shift in the dominant wave energy towards longer wavelengths of 80 m. This is illustrated at locations B (Fig.13b), E (Fig.13e), and H (Fig.13h). Collectively, the oil slicks dampen the wave energy at short wavelengths, and the oil slicks are more detectable under a weak sea state.

5 Summary and Conclusions

Accidental oil spills from ships are a major marine disaster in near-shore waters (Sergievskaya *et al.*, 2019). Remote-sensing satellites are powerful tools for oil spill mon-

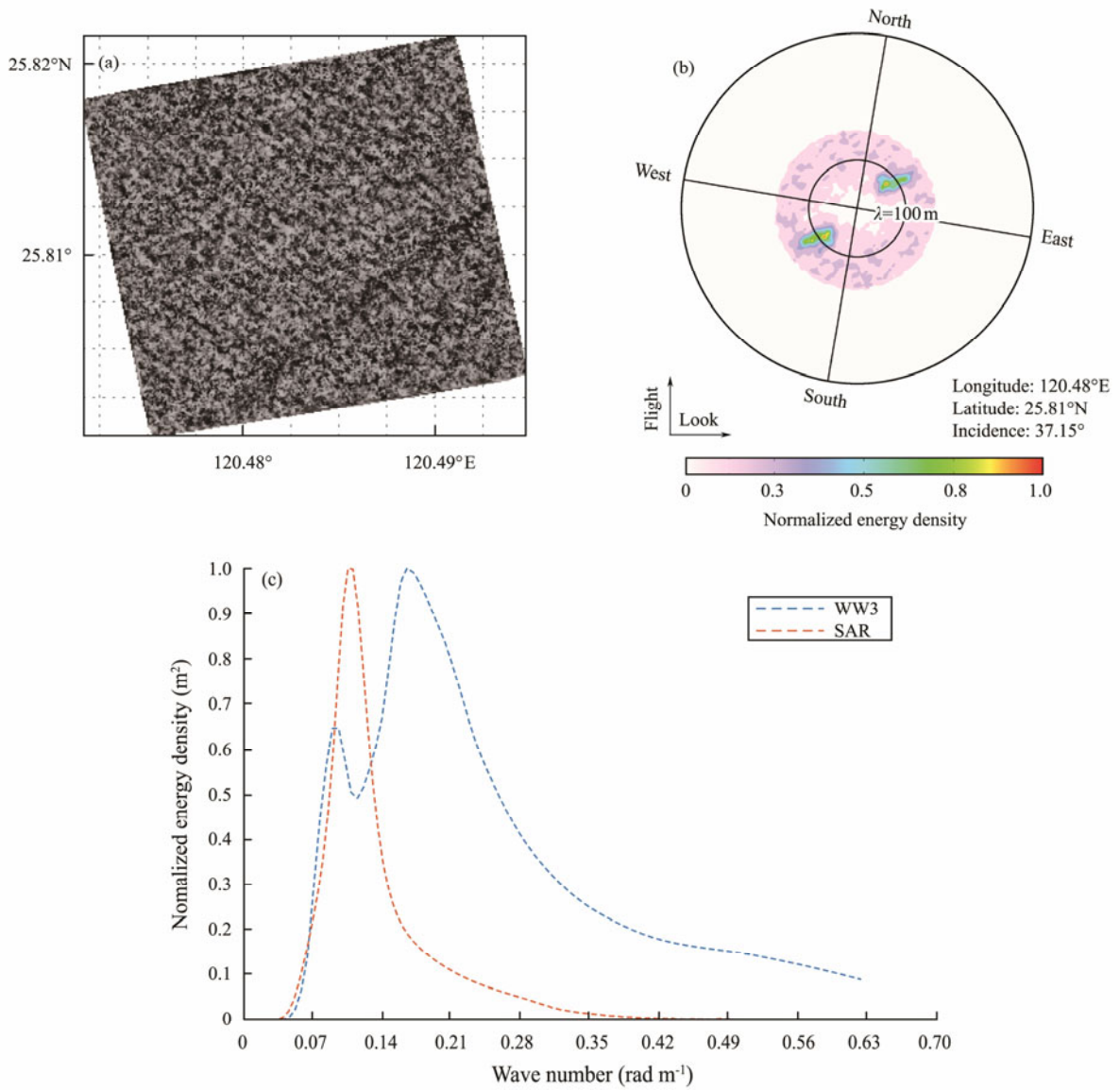

Fig.9 (a) The sub-scene extracted from the images taken on June 16, 2007, at 05:43 UTC; (b) the corresponding two-dimensional SAR spectrum; and (c) the inverted one-dimensional wave spectrum obtained using the PFSM algorithm (red dashed line) and the WW3-simulated wave spectrum (blue dashed line).

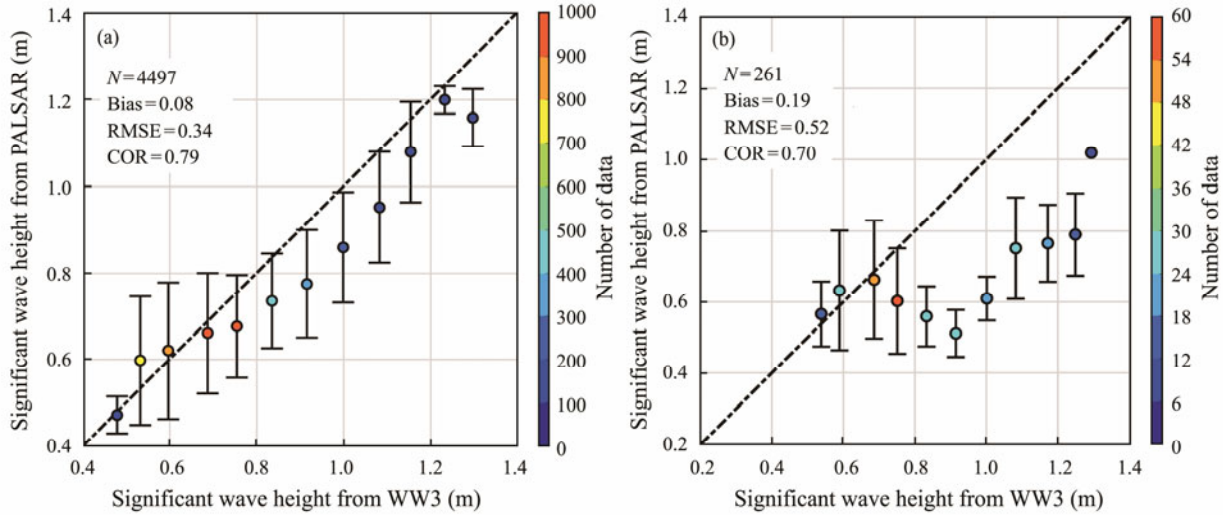

Fig.10 Comparisons between the SAR-derived SWH obtained from the PALSAR images using the PFSM algorithm and the collocated simulations from the WW3 model for a 0.1 m bin (a) in the regions without oil slicks and (b) in the regions with oil slicks.

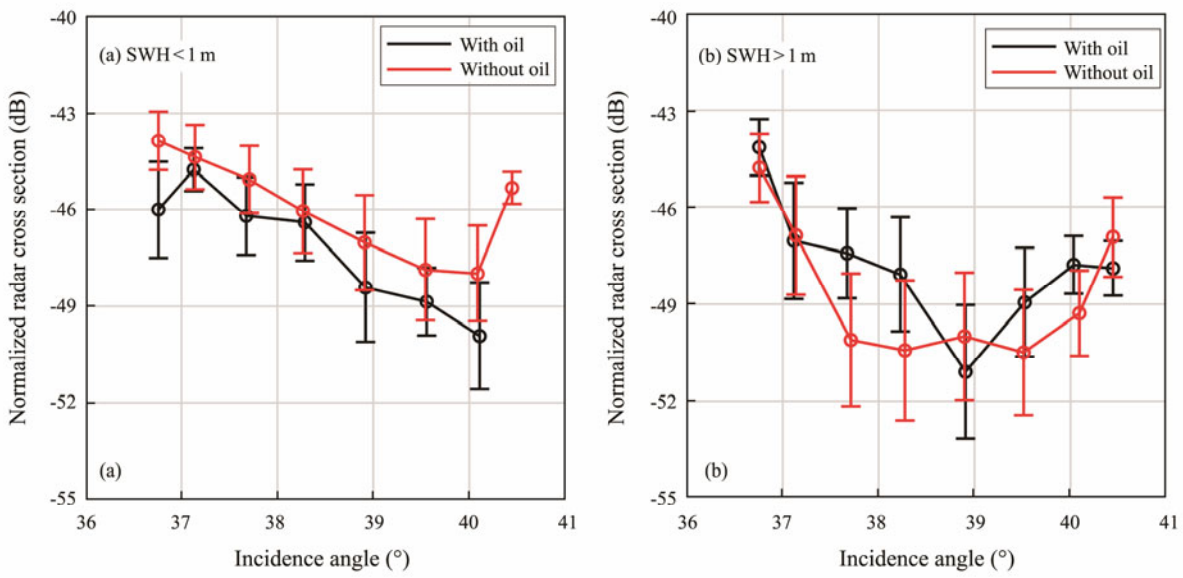

Fig.11 The relationships between the incidence angle and SAR-measured NRCS for the clean sea surface (red lines) and oil covered surface (black lines): (a) SWH < 1 m; (b) SWH > 1 m.

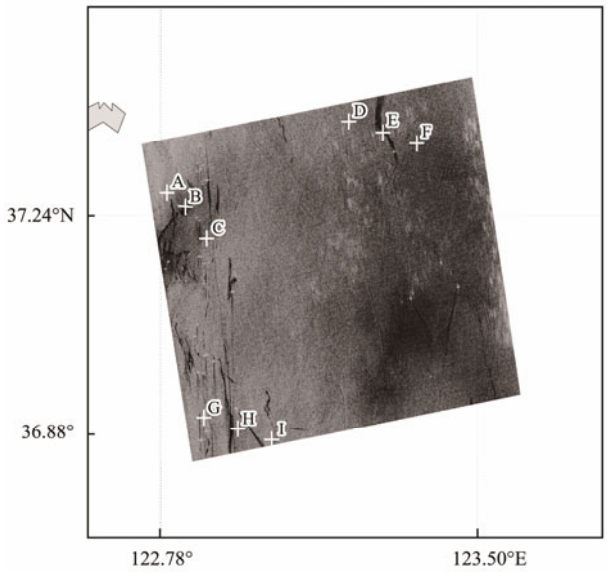

Fig.12 The quick-look of the PALSAR images taken on July 17, 2017, at 14:14 UTC, in which spots A–I were selected to analyze the wave retrieval results as the wave passed through the oil slicks.

itoring. Due to its fine resolution, SAR is particularly useful (Velotto *et al.*, 2011). Most previous studies have focused on detecting oil slicks using SAR images (Nunziata *et al.*, 2018) and predicting the behavior of spilled oil using a numerical dynamics model (Price *et al.*, 2006). Since oil slicks modulate the sea surface roughness, they could affect the wave retrieval for SAR. Therefore, the main purpose of this study was to investigate the results of the waves as they pass through oil slicks using 20 PALSAR images from ALOS-1. The HH-polarized GMF LMOD was used for the wind retrieval from the collected PALSAR images. Because the SAR-measured wind directions have a 180° ambiguity, 0.25° gridded ERA-5 winds were used to remove this ambiguity. The SAR-derived wind speeds were inverted from the PALAR images using the prior information about the wind directions in the GMF LMOD. The validation of the SAR-derived wind speeds for about 1000 matchups with ASCAT-measured winds produced a 1.82 m s^{-1} RMSE for the wind speed and a COR of 0.86. With respect to the effect of the oil slicks on the wind retrieval, comparisons with 0.25° gridded ERA-5 winds produced an RMSE and COR for the wind speed of 1.90 m s^{-1} and 0.84, respectively, for the regions without oil slicks, which are lower and higher than the RMSE and COR of 2.70 m s^{-1} and 0.64, respectively, for the regions with oil slicks. The underestimation (>1 m s^{-1}) of the SAR-derived wind speeds was particularly obvious when the wind speeds were greater than 5 m s^{-1}. This issue probably led to the underestimation of the SAR-derived SWH, indicating that the accuracy of the winds used in the wave retrieval process could affect the accuracy of the retrieved SWH. Moreover, a large difference in the SWH (about 0.2 m) was achieved when comparing the SAR-derived and WW3-simulated SWHs for the regions with oil slicks. Three profiles passing through the oil slicks were analyzed in order to investigate the effects of the oil slicks on SAR-derived wave spectrum compared with those from the WW3 model. We found that short wavelengths (<30 m) were dampened by the oil slicks, and thus, the dominant wave spectra shifted toward longer wavelengths (about 80 m). We also found that oil spills are more detectable under weak sea states (SWH < 1 m). and thus, the dominant wave spectra shifted toward longer wavelengths (about 80 m). We also found that oil spills are more detectable under weak sea states (SWH < 1 m).

The oil particle drift mainly depends on the ocean dynamics, *e.g.*, sea-surface winds, tides, and circulation currents (Sun *et al.*, 2018). Therefore, the real-time winds and waves derived from SAR images are useful for improving the accuracy of tracking simulations using the oil particle-tracing method.

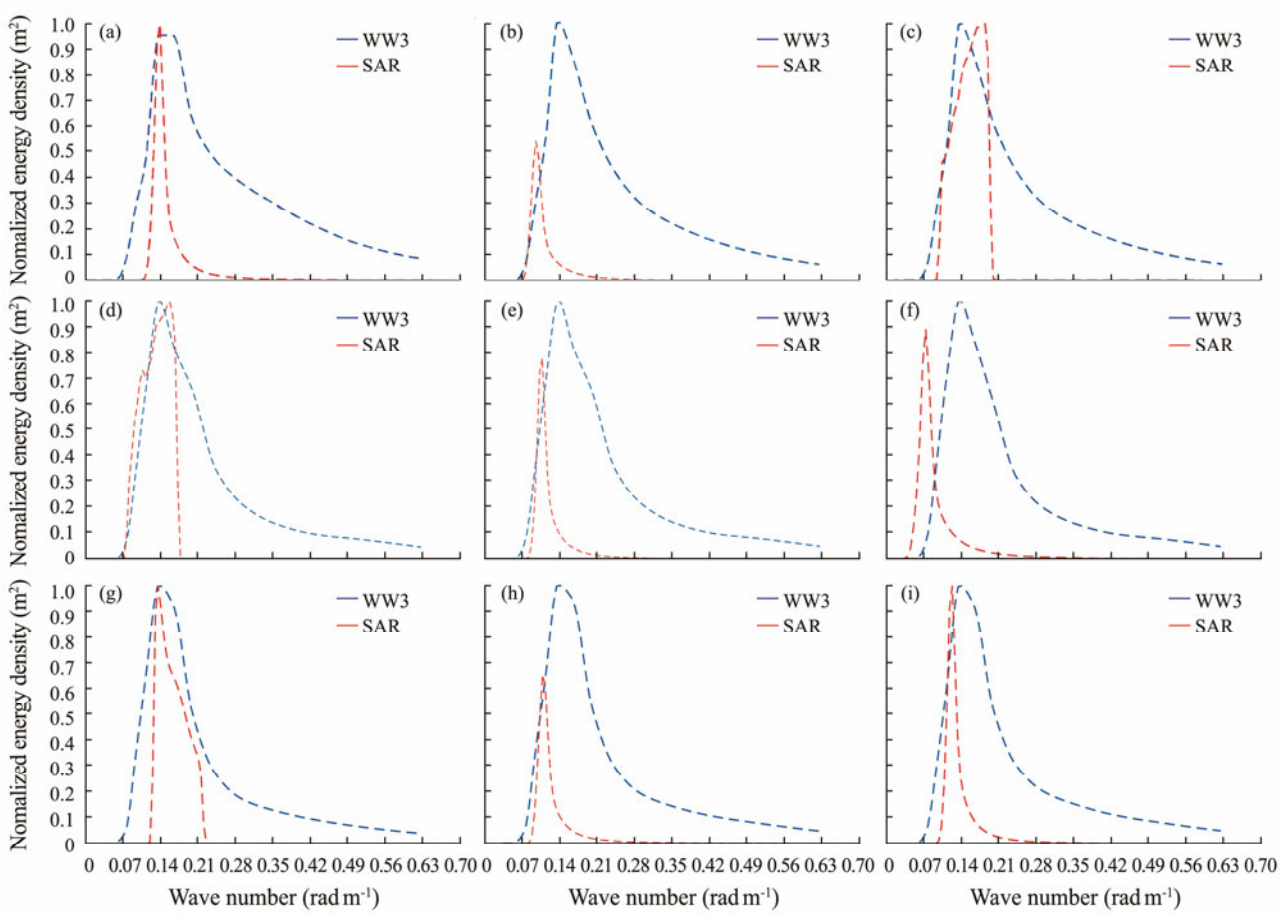

Fig.13 The one-dimensional wave spectra inverted from the sub-scenes at the locations in Fig.12, in which (a)−(i) correspond to A−I.

Acknowledgements

This research was partly supported by the National Natural Science Foundation of China (Nos. 41906152 and 42076238). We greatly appreciate the National Center for Environmental Prediction of the National Oceanic and Atmospheric Administration for providing the source code for the WAVEWATCH-III model free of charge. The European Centre for Medium-Range Weather Forecasts wind data were accessed *via* http://www.ecmwf.int. The General Bathymetry Chart of the Oceans (GEBCO) data were downloaded from ftp.edcftp.cr.usgs.gov. The operational Geophysical Data Record (OGDR) wave data following the footprints of the Jason-2 altimeter were downloaded from https://data.nodc.noaa.gov. The Advanced Scatterometer 25 km wind products provided by the Royal Netherlands Meteorological Institute were downloaded from http://archive.eumetsat.int. We would also like to thank the Aerospace Information Research Institute for providing the historical Advanced Land Observing Satellite images.

References

Alpers, W., and Brummer, B., 1994. Atmospheric boundary layer rolls observed by the synthetic aperture radar aboard the ERS-1 satellite. *Journal of Geophysical Research*, **99** (C6): 2613-2621, DOI: 10.1029/94JC0042.

Alpers, W., Ross, D., and Rufenach, C., 1981. On the detectability of ocean surface waves by real and synthetic radar. *Journal of Geophysical Research*, **86** (C7): 6481-6498, DOI: 10.1029/JC086iC07p06481.

Bi, L., Jung, J. A., Morgan, M. C., and Le Marshall, J. F., 2011. Assessment of assimilating ASCAT surface wind retrievals in the NCEP global data assimilation system. *Monthly Weather Review*, **139** (11): 3405-3421, DOI: 10.1175/2011MWR3391.1.

Ding, Y. Y., Zuo, J. C., Shao, W. Z., Shi, J., Yuan, X. Z., Sun, J., *et al.*, 2019. Wave parameters retrieval for dual-polarization C-band synthetic aperture radar using a theoretical-based algorithm under cyclonic conditions. *Acta Oceanologica Sinica*, **38** (5): 21-31, DOI: 10.1007/s13131-019-1438-y.

Ermakov, S. A., Sergievskaya, I. A., and Gushchin, L. A., 2012. Damping of gravity-capillary waves in the presence of oil slicks according to data from laboratory and numerical experiments. *Izvestiya Atmospheric and Oceanic Physics*, **48** (7): 565-572, DOI: 10.1134/S000143381204007X.

Esaias, W. E., Abbott, M. R., Barton, I., Brown, O. B., Campbell, J. W., Carder, K. L., *et al.*, 1998. An overview of MODIS capabilities for ocean science observations. *IEEE Transactions on Geoscience and Remote Sensing*, **36** (4): 1250-1265, DOI: 10.1109/36.701076.

Feindt, F., Schroter, J., and Alpers, W., 1986. Measurement of the ocean wave-radar modulation transfer function at 35 GHz from a sea-based platform in the North Sea. *Journal of Geophysical Research*, **91** (C8): 9701-9708, DOI: 10.1029/JC091iC08p09701.

Grieco, G., Lin, W., Migliaccio, M., Nirchio, F., and Portabella, M., 2016. Dependency of the Sentinel-1 azimuth wavelength

cut-off on significant wave height and wind speed. *International Journal of Remote Sensing*, **37** (21): 5086-5104, DOI: 10.1080/01431161.2016.1226525.

Hasselmann, K., 1973. Measurements of wind-wave growth and swell decay during the Joint North Sea Wave Project (JONSWAP). *Deutches Hydrographisches Institut*, **12** (2): 1-95, DOI: citeulike-article-id:2710264.

Hasselmann, K., and Hasselmann, S., 1991. On the nonlinear mapping of an ocean wave spectrum into a synthetic aperture radar image spectrum. *Journal of Geophysical Research*, **96** (C5): 10713-10729, DOI: 10.1029/91JC00302.

He, Y. J., Shen, H., and Perrie, W., 2006. Remote sensing of ocean waves by polarimetric SAR. *Journal of Atmospheric and Oceanic Technology*, **23** (12): 1768-1773, DOI: 10.1175/JTECH1948.1.

Hersbach, H., 2010. Comparison of C-band scatterometer CMOD5.N equivalent neutral winds with ECMWF. *Journal of Atmospheric and Oceanic Technology*, **27** (4): 721-736, DOI: 10.1175/2009JTECHO698.1.

Hersbach, H., Stoffelen, A., and Haan, S., 2007. An improved C-band scatterometer ocean geophysical model function: CMOD5. *Journal of Geophysical Research*, **112** (C3): 225-237, DOI: 10.1029/2006JC003743.

Honkavaara, E., Saari, H., Kaivosoja, J., Pölönen, I., and Pesonen, L., 2013. Processing and assessment of spectrometric, stereoscopic imagery collected using a lightweight UAV spectral camera for precision agriculture. *Remote Sensing*, **5** (10): 5006-5039, DOI: 10.3390/rs5105006.

Hu, Y. Y., Shao, W. Z., Shi, J., Sun, J., Ji, Q. Y., and Cai, I. N., 2020a. Analysis of the typhoon wave distribution simulated in WAVEWATCH-III model in the context of Kuroshio and wind-induced current. *Journal of Oceanology and Limnology*, **38** (1): 1692-1710, DOI: 10.1007/s00343-019-9133-6.

Hu, Y. Y., Shao, W. Z., Wei, Y. L., and Zuo, J. C., 2020b. Analysis of typhoon-induced waves along typhoon tracks in the western North Pacific Ocean, 1998–2017. *Journal of Marine Science and Engineering*, **8** (7): 521, DOI: 110.3390/jmse8070521.

Isoguchi, O., and Shimada, M., 2009. An L-band ocean geophysical model function derived from PALSAR. *IEEE Transactions on Geoscience and Remote Sensing*, **47** (7): 1925-1936, DOI: 10.1109/TGRS.2008.2010864.

Jakobsson, M., and Macnab, R., 2006. A comparison between GEBCO sheet 5.17 and the international bathymetric chart of the Arctic Ocean (IBCAO) version 1.0. *Marine Geophysical Researches*, **27** (1): 35-48, DOI: 10.1007/s11001-005-7760-0.

Kudryavtsev, V., Hauser, D., Caudal, G., and Chapron, B., 2003. A semiempirical model of the normalized radar cross section of the sea surface, 2. Radar modulation transfer function. *Journal of Geophysical Research*, **108** (C3): FET31-FET316, DOI: 10.1029/2001JC001004.

Lehner, S., Horstmann, J., Koch, W., and Rosenthal, W., 1998. Mesoscale wind measurements using recalibrated ERS SAR images. *Journal of Geophysical Research*, **103**: 7847-7856, DOI: 10.1029/97JC02726.

Li, X. M., and Lehner, S., 2014. Algorithm for sea surface wind retrieval from TerraSAR-X and TanDEM-X data. *IEEE Transactions on Geoscience and Remote Sensing*, **52** (5): 2928-2939, DOI: 10.1109/TGRS.2013.2267780.

Li, X. M., Zhang, T. Y., Huang, B. Q., and Jia, T., 2018. Capabilities of Chinese Gaofen-3 synthetic aperture radar in selected topics for coastal and ocean observations. *Remote Sensing*, **10** (12): 1929, DOI: 110.3390/rs10121929.

Li, X., Lehner, S., and Bruns, T., 2011. Ocean wave integral parameter measurements using Envisat ASAR wave mode data. *IEEE Transactions on Geoscience and Remote Sensing*, **49** (1): 155-174, DOI: 10.1109/TGRS.2010.2052364.

Lyzenga, D., 1986. Numerical simulation of synthetic aperture radar image spectra for ocean waves. *IEEE Transactions on Geoscience and Remote Sensing*, GE-**24** (6): 863-872, DOI: 10.1109/TGRS.1986.289701.

Lyzenga, D., 2002. Unconstrained inversion of wave height spectra from SAR images. *IEEE Transactions on Geoscience and Remote Sensing*, **40** (2): 261-270, DOI: 10.1109/36.992783.

Mastenbroek, C., and Valk, C., 2000. A semi-parametric algorithm to retrieve ocean wave spectra from synthetic aperture radar. *Journal of Geophysical Research*, **105** (C2): 3497-3516, DOI: 10.1029/1999JC900282.

Meng, T. Y., Yang, X. F., Chen, K. S., Nunziata, F., Xie, D. F., and Buono, A., 2022. Radar backscattering over sea surface oil emulsions: Simulation and observation. *IEEE Transactions on Geoscience and Remote Sensing*, **60**: 1-14, DOI: 10.1109/TGRS.2021.3073369.

Migliaccio, M., Huang, L., and Buono, A., 2019. SAR speckle dependence on ocean surface wind field. *IEEE Transactions on Geoscience and Remote Sensing*, **57** (8): 5447-5455, DOI: 10.1109/TGRS.2019.2899491.

Monaldo, F., Jackson, C., Li, X. F., and Pichel, W., 2016. Preliminary evaluation of Sentinel-1A wind speed retrievals. *IEEE Journal of Selected in Applied Earth Observations and Remote Sensing*, **9** (6): 2638-2642, DOI: 10.1109/JSTARS.2015.2504324.

Mouche, A. A., Hauser, D., Daloze, J. F., and Guerin, C., 2005. Dual polarization measurements at C-band over the ocean: Results from airborne radar observations and comparison with ENVISAT ASAR data. *IEEE Transaction on Geoscience and Remote Sensing*, **43** (4): 753-769, DOI: 10.1109/TGRS.2005.843951.

Nunziata, F., De Macedo, C. R., Buono, A., Velotto, D., and Migliaccio, M., 2018. On the analysis of a time series of X-band Terrasar-X SAR imagery over oil seepages. *International Journal of Remote Sensing*, **40** (9): 3623-3646, DOI: 10.1080/01431161.2018.1547933.

Pleskachevsky, A., Rosenthal, W., and Lehner, S., 2016. Meteo-Marine parameters for highly variable environment in coastal regions from satellite radar images. *ISPRS Journal of Photogrammetry and Remote Sensing*, **119** (2): 464-484, DOI: 10.1016/j.isprsjprs.2016.02.001.

Price, J. M., Reed, M., Howard, M. K., Johnson, W. R., Ji, Z. G., Marshall, C. F., *et al.*, 2006. Preliminary assessment of an oil-spill trajectory model using satellite-tracked, oil-spill-simulating drifters. *Environmental Modelling and Software*, **21** (2): 258-270, DOI: 10.1016/j.envsoft.2004.04.025.

Quilfen, Y., Chapron, B., Elfouhaily, T., Katsaros, K., and Tournadre, J., 1998. Observation of tropical cyclones by high-resolution scatterometry. *Journal of Geophysical Research*, **103** (C4): 7767-7786, DOI: 10.1029/97JC01911.

Schulz-Stellenfleth, J., Konig, T., and Lehner, S., 2007. An empirical approach for the retrieval of integral ocean wave parameters from synthetic aperture radar data. *Journal of Geophysical Research*, **112** (C3): 10182-10190, DOI: 10.1029/2006JC003970.

Sergievskaya, I., Ermakov, S., Lazareva, T., and Guo, J., 2019. Damping of surface waves due to crude oil/oil emulsion films on water. *Marine Pollution Bulletin*, **146** (9): 206-214, DOI: 10.1016/j.marpolbul.2019.06.018.

Shao, W. Z., Hu, Y. Y., Yang, J., Nunziata, F., Sun, J., and Li, H., *et al.*, 2018a. An empirical algorithm to retrieve significant wave height from Sentinel-1 synthetic aperture radar imagery

collected under cyclonic conditions. *Remote Sensing*, **10** (9): 1367, DOI: 10.3390/rs10091367.

Shao, W. Z., Li, X. F., and Sun, J., 2015. Ocean wave parameters retrieval from TerraSAR-X images validated against buoy measurements and model results. *Remote Sensing*, **7** (10): 12815-12828, DOI: 10.3390/rs71012815.

Shao, W. Z., Li, X. M., Lehner, S., and Guan, C. L., 2014a. Development of polarization ratio model for sea surface wind field retrieval from TerraSAR-X HH polarization data. *International Journal of Remote Sensing*, **35** (11-12): 4046-4063, DOI: 10.1080/01431161.2014.916059.

Shao, W. Z., Nunziata, F., Zhang, Y. G., Corcione, V., and Migliaccio, M., 2021. Wind speed retrieval from the Gaofen-3 synthetic aperture radar for VV- and HH-polarization using a retuned algorithm. *European Journal of Remote Sensing*, **54** (1): 318-337, DOI: 10.1080/22797254.2021.1924082.

Shao, W. Z., Sheng, Y. X., Li, H., Shi, J., Ji, Q. Y., Tan, W., *et al.*, 2018b. Analysis of wave distribution simulated by WAVEWATCH-III model in typhoons passing Beibu Gulf, China. *Atmosphere*, **9** (7): 265-284, DOI: 10.3390/atmos9070265.

Shao, W. Z., Sun, J., Guan, C. L., and Sun, Z. F., 2014b. A method for sea surface wind field retrieval from SAR image mode data. *Journal of Ocean University of China*, **13** (2): 198-204, DOI: 10.1007/s11802-014-1999-5.

Shao, W. Z., Yu, W. P., Jiang, X. W., Shi, J., Wei, Y. L., and Ji, Q. Y., 2022. Analysis of wave distribution using WAVEWATCH-III model in the Arctic Ocean. *Journal of Ocean University of China*, **21** (1): 15-27, DOI: 10.1007/s11802-022-4811-y.

Shao, W. Z., Zhu, S., Sun, J., Yuan, X. Z., Sheng, Y. X., Zhang, Q. J., *et al.*, 2018c. Evaluation of wind retrieval from co-polarization Gaofen-3 SAR imagery around China Seas. *Journal of Ocean University of China*, **18** (1): 80-92, DOI: 10.1007/s11802-019-3779-8.

Sheng, Y. X., Shao, W. Z., Zhu, S., Sun, J., Yuan, X. Z., Li, S. Q., *et al.*, 2018. Validation of significant wave height retrieval from co-polarization Chinese Gaofen-3 SAR imagery by using an improved algorithm. *Acta Oceanologica Sinica*, **37** (6): 302-315, DOI: 10.1007/s13131-018-1217-1.

Shimada, M., Lsoguchi, O., Tadono, T., and Isono, K., 2009. PALSAR radiometric and geometric calibration. *IEEE Transactions on Geoscience and Remote Sensing*, **47** (12): 3915-3932, DOI: 10.1109/TGRS.2009.2023909.

Shimada, T., Kawamura, H., and Shimada, M., 2003. An L-band geophysical model function for SAR wind retrieval using JERS-1 SAR. *IEEE Transactions on Geoscience and Remote Sensing*, **41** (3): 518-531, DOI: 10.1109/TGRS.2003.808836.

Shulz-Stellenfleth, J., Lehner, S., and Hoja, D., 2005. A parametric scheme for the retrieval of two-dimensional ocean wave spectra from synthetic aperture radar look cross spectra. *Journal of Geophysical Research*, **110** (C5): C05004, DOI: 10.1029/2004JC002822.

Stoffelen, A., and Anderson, D., 1997. Scatterometer data interpretation estimation and validation of the CMOD4. *Journal of Geophysical Research*, **102** (102): 5767-5780, DOI:10.1029/96JC02860.

Stoffelen, A., Verspeek, J. A., Vogelzang, J., and Verhoef, A., 2017. The CMOD7 geophysical model function for ASCAT and ERS wind retrievals. *IEEE Journal of Selected Topics in Applied Earth Observations and Remote Sensing*, **10** (5): 2123-2134, DOI: 10.1109/JSTARS.2017.2681806.

Stopa, J., and Mouche, A., 2017. Significant wave heights from Sentinel-1 SAR: Validation and applications. *Journal of Geophysical Research*, **122** (3): 1827-1848, DOI: 10.1002/2016JC012364.

Sun, J., and Kawamura, H., 2009. Retrieval of surface wave parameters from SAR images and their validation in the coastal seas around Japan. *Journal of Oceanography*, **65** (4): 567-577, DOI: 10.1007/s10872-009-0048-2.

Sun, S., Lu, Y., Liu, Y., Wang, M., and Hu, C., 2018. Tracking an oil tanker collision and spilled oils in the East China Sea using multisensor day and night satellite imagery. *Geophysical Research Letters*, **45** (7): 3212-3220, DOI: 10.1002/2018GL077433.

The Wamdi Group, 1988. The WAM model – A third generation ocean wave prediction model. *Journal of Physical Oceanography*, **18** (12): 1775-1810, DOI: 10.1175/1520-0485(1988)018<1775:TWMTGO>2.0.CO;2.

Tolman, H., and Chalikov, D., 1996. Source terms in a third-generation wind wave model. *Journal of Physical Oceanography*, **26** (11): 2497-2518, DOI: 10.1175/1520-0485(1996)0262.0.CO;2.

Velotto, D., Migliaccio, M., Nunziata, F., and Lehner, S., 2011. Dual-polarized TerraSAR-X data for oil-spill observation. *IEEE Transactions on Geoscience and Remote Sensing*, **49** (12): 4751-4762, DOI: 10.1109/TGRS.2011.2162960.

Verspeek, J., Stoffelen, A., Portabella, M., Bonekamp, H., Anderson, C., and Saldana, J. F., 2010. Validation and calibration of ASCAT using CMOD5.N. *IEEE Transactions on Geoscience and Remote Sensing*, **48** (1): 386-395, DOI: 10.1109/TGRS.2009.2027896.

Voorrips, C., Mastenbroek, C., and Hansen, B., 2001. Validation of two algorithms to retrieve ocean wave spectra from ERS synthetic aperture radar. *Journal of Geophysical Research: Atmospheres*, **106** (C8): 16825-16840, DOI: 10.1029/1999JC000156.

Yang, X. F., Li, X. F., Zheng, Q. A., Gu, X. F., Pichel, W. G., and Li, Z. W., 2011. Comparison of ocean surface winds retrieved from QuikSCAT scatterometer and Radarsat-1 SAR in offshore waters of the U.S. west coast. *IEEE Geoscience and Remote Sensing Letters*, **8** (1): 163-167, DOI: 10.1109/LGRS.2010.2053345.

Yang, Z. H., Shao, W. Z., Hu, Y. Y., Ji, Q. Y., and Zhou, W., 2021. Revisit of a case study of spilled oil slicks caused by the Sanchi accident (2018) in the East China Sea. *Journal of Marine Science and Engineering*, **9** (3): 279, DOI: 110.3390/jmse9030279.

Zhang, B., Perrie, W., and He, Y. J., 2010. Validation of RADARSAT-2 fully polarimetric SAR measurements of ocean surface waves. *Journal of Geophysical Research*, **116** (C6): 302-315, DOI: 10.1029/2009JC005887.

Zheng, H., Zhang, Y., Wang, Y., Zhang, X., and Meng, J., 2017. The polarimetric features of oil spills in full polarimetric synthetic aperture radar images. *Acta Oceanologica Sinica*, **36** (5): 105-114, DOI: 10.1007/s13131-017-1065-4.

Zhu, S., Shao, W. Z., Armando, M., Shi, J., Sun, J., Yuan, X. Z., *et al.*, 2019. Evaluation of Chinese quad-polarization Gaofen-3 SAR wave mode data for significant wave height retrieval. *Canadian Journal of Remote Sensing*, **44** (6): 588-600, DOI: 10.1080/07038992.2019.1573136.

(Edited by Xie Jun)